Capillary imbibition in open-cell monodisperse foams

Olivier Pitois, Asmaa Kaddami, Vincent Langlois

Capillary imbibition in open-cell monodisperse foams

Olivier Pitois*, Asmaa Kaddami and Vincent Langlois.

Lab Navier, Univ Gustave Eiffel, ENPC, CNRS, F-77447 Marne-la-Vallée, France.

* Corresponding author:
Olivier Pitois
Lab Navier, Univ Gustave Eiffel, ENPC, CNRS, F-77447 Marne-la-Vallée, France.
33 1 81 66 84 51
olivier.pitois@ifsttar.fr

Abstract:

Hypothesis: Although capillary imbibition of solid foams is involved in many industrial applications, general theory for capillary imbibition has never been proved to apply for this specific class of porous materials.

Experiments: In order to compare accurately experiment and theory we produce solid foam samples with monodisperse pore size distributions and tunable pore volume fraction, and we measure their permeability (Darcy), their capillary pressure and their imbibition rate.

Findings: Our findings reveal that the imbibition velocity is qualitatively compatible with the Washburn theory but it is one order of magnitude smaller than the predicted value. This deviation is attributed to the excess time spent by the liquid-gas interface through connections between pores, for which an empirical expression is provided as a function of pore size and solid volume fraction. Our results provide the first step to understand deeply the imbibition process in foams and to predict imbibition rates for various foamed materials.

Keywords : porous media; fluid flows; permeability; foam

1. Introduction

Solid foams are widely used from years in many different fields thanks to their large specific surface area, low density, mechanical properties and thermal/acoustic insulation efficiency [1]. Liquid capillary imbibition occurs in solid foams, either as wanted process or as unexpected event. For example, clean-up of oily pollution and oil-water separation can be performed by using solid foams. In such a case, oil is sucked by the foam whose surface has been made hydrophobic [2,3]. Food industry uses increasingly dried foamed products which have to be imbibed and dissolved in water [4]. Imbibition is required for impregnation purpose with simple or complex fluids in order to modify the properties of the foam surface. This increases drastically the spectrum of properties which can be given to foams, i.e. superhydrophobicity [5,6], antibacterial [7], electrical [8] or fire-safe [9] properties. On a different note, durability of foamed construction materials can be jeopardized by successive imbibition/drying cycles. Therefore, controlling sorption properties of those materials is a crucial issue and water repellents can be used for preventing or decreasing water absorption [10].

For each example given above, the rate at which the porous material can be filled due to capillary imbibition is a crucial aspect, and theoretical prediction of the imbibition kinetics is of great interest. Said in another way, designing materials with appropriate imbibition properties requires understanding how sorption behavior depends on the material's morphology. Theory of capillary imbibition has been intensively studied from the pioneering works of Bell & Cameron [11], Lucas [12] and Washburn [13]. They assumed that a wet front progresses through the sample under the action of capillary suction while saturating the material behind. Such a basic theory has to be modified to account for the specific microstructure encountered in various porous materials [14]. It is to say that such a specific work has not been performed to date for solid foams.

We investigate the imbibition behavior of solid foams characterized by independent pore size and solid volume fractions. The results allow for a consistent description of the capillary imbibition process in foams. Theory of capillary imbibition is presented in section 2. Foam samples are produced and characterized in section 3. Imbibition results are presented and discussed in section 4.

2. Theory

Let us briefly recall the classical theory for capillary imbibition of liquids through porous media. Here is considered the vertical capillary rise of liquid at height $h(t)$ through a porous material with porous volume fraction ϕ. By introducing the mean curvature for the water interface in the pores, $1/\bar{r}$, the driving capillary pressure is given by the Laplace law: $\Delta P_c = 2\sigma/\bar{r}$. Note that in the following

we consider the driving pressures as positive values, i.e. $\Delta P_c = |2\sigma/\bar{r}|$. The progression of the interface at height h is restrained by gravity, so the effective driving pressure is $\Delta P = \Delta P_c - \rho g h(t)$. The resulting interface velocity v_I $(= dh/dt)$ can be estimated via the Darcy law: $V_D = k_I/\mu \times \Delta P/h$, where μ is the fluid dynamic velocity, k_I the permeability, and V_D $(= \phi v_I)$ the Darcy velocity. The equation for the evolution of the interface height is therefore:

$$v_I = \frac{k_I \Delta P_c}{\phi \mu}\frac{1}{h} - \frac{\rho g k_I}{\phi \mu} = \frac{a}{h} - b \quad \text{(eq. 1)}$$

where the parameters $a = \frac{\Delta P_c k_I}{\phi \mu}$ et $b = \frac{\rho g k_I}{\phi \mu}$ have been introduced. Note that the ratio a/b corresponds to the Jurin height: $h_\infty = \Delta P_c/\rho g$. The solution of equation (1) is given by [13]:

$$t = -\frac{h}{b} - \frac{a}{b^2} ln\left(1 - \frac{bh}{a}\right) \quad \text{(eq. 2)}$$

Note also that equation (1) simplifies for $h \ll h_\infty$ and the Washburn solution can be conveniently used:

$$v_I \cong \frac{a}{h} = \frac{k_I \Delta P_c}{\phi \mu}\frac{1}{h} \quad \text{(eq. 3)}$$

$$h \cong (2at)^{1/2} = \left(\frac{2k_I \Delta P_c}{\phi \mu} t\right)^{1/2} \quad \text{(eq. 4)}$$

3. Production and characterization of the solid foam samples

Studied solid foams are geopolymer foams produced from metakaolin (MK) particles by using a dedicated process presented in the following.

3.1. Materials

We used an activating solution prepared by mixing NaOH solution (mass concentration C_w = 0.35) with a solution containing Na_2O (C_w = 0.08) and SiO_2 (C_w = 0.27) provided by MERCK KGaA, and water. The density is ρ_ℓ = 1400 kg/m^3 and the chemical composition is given by molar ratios H_2O/Na_2O = 14.68 and SiO_2/Na_2O = 1.01.

Metakaolin (MK) particles were provided by AGS Minéraux (France): Argical M 1200s. Chemical compositions: SiO_2 55.0%, Al_2O_3 39.0%, Fe_2O_3 1.8%, TiO_2 1.5%, K_2O+Na_2O 1.0%, CaO+MgO 0.6%. As provided by the supplier: BET specific surface area is equal to 19 m^2/g and mass average diameter is approximately $d_p \approx 2$ µm. Their density is ρ_{MK} = 2200 kg/m^3.

The activated MK suspensions were prepared by mixing a mass m_ℓ of the activating solution with a mass m_{MK} of metakaolin particles. The suspension is characterized by the ratio $L/S = m_\ell/m_{MK}$. For the present study L/S was within the range 1.75-2. The chemical composition of those samples is given by Si/Al and Na_2O/Al_2O_3 ratios, respectively within the ranges 1.8-2.5 and 1.2-2.7. The typical setting time is about two hours.

Glucopon® 225 DK (alkyl polyglycoside provided by BASF) was used as surfactant for foaming purpose. Surface tension of Glucopon water solutions was measured (using a pendant drop tensiometer) to be σ = 30 mN/m for concentrations above the critical micellar concentration. Dynamic viscosity of such water solutions is very close to that of pure water, i.e. $\mu \cong 10^{-3}$ Pa.s. Such a nonionic surfactant of molar mass equal to 420 g/mol was shown to be suitable to stabilize the foam morphology during the two hours preceding the geopolymerization stage.

3.2. Production

The method used for the production of controlled MK foams has been presented in a previous paper [15]. Here we recall the main steps but the reader can refer to [15] for more details.

In broad outline, metakaolin foams were produced by mixing precursor aqueous foam with the metakaolin (MK) suspension described previously. The production process consists of two steps: (1) production of the precursor aqueous foam, (2) mixing of the precursor aqueous foam with the MK suspension and in-line filling of the resulting MK fresh foam in a vessel.

Step 1: Aqueous foam was generated by pushing both gas (nitrogen) and foaming liquid (glucopon water solution) through a T-junction. Tuning the gas/liquid flow rates ratio allowed producing monodisperse bubbles with chosen diameters ranging between 200 µm and few millimeters. Generated bubbles were continuously collected into a vertical glass column. The average bubble diameter D_b was measured using a camera focused at the wall of the column. For foam made with bubble size $D_b \gtrsim 500$ µm, ripening turned out to be insignificant over the duration of the production step, so highly monodisperse precursor aqueous foams were obtained. In contrast, smaller bubble sizes were observed to evolve during the production step because of the ripening

process. This can be explained by both the increase of the ripening rate for smaller bubbles [16] and the decrease of the production rate (larger time required to produce the same volume of foam) for smaller bubbles. Such an evolution was efficiently counteracted by using perfluorohexane as a saturating vapor in the bubbling gas [17].

Step 2: After production of the required precursor foam volume, the latter was pushed with the MK suspension through a static mixer (flow focusing device and classical helical geometries). The gas volume fraction within the resulting MK foam could be adjusted by tuning the ratio of flow rates for the precursor foam and the MK suspension. The resulting fresh foam was continuously pushed in a sample vessel of diameter 26 mm and height H_0 = 50 mm. Typical volume flow rates for the production of the studied samples were of the order of 10 mL/min. The vessel was filled to the top and closed. Note that the values for the solid volume fraction ϕ_s were also determined a posteriori by comparing the measured density of the fresh MK foam with the density of the MK suspension. After 2 days in the closed vessels, samples were let for drying at room temperature for 2 days before unmolding.

3.3. Foam microstructure

Optical microscopy (see Figure 1c) was used to observe the foam structure and to measure the size of both pores and apertures that connect them. In such a case, mean values (over $\approx$ 100 measurements) will be reported.

In addition, X-ray tomography (EasyTom RX Solutions) was used to obtain size distributions. Images of small samples (i.e. 5x5x10 mm) were obtained with a Ultratom scanner from RX solutions. Measurement involved a Hamamatsu L10801 X-ray source (160 kV) and a Paxscan Varian 2520 V at-panel imager. All scans were performed at 60 kV and 85 µA. Frame rate was 3 images per second and 12 images were averaged to produce one projection (the resulting effective exposure time was therefore 4s). 3D tomographic reconstruction was performed with the X-Act commercial software developed by RX-Solutions. Voxel size for the obtained images was 5 µm. Pores appeared black on the reconstructed images and interstitial geopolymer solid was light grey. This allowed us to analyze the images with the freeware ImageJ program [18] to compute the pore size distribution: First, a closing filter from MorphoLibJ plugin [19] with a 2 voxel-radius ball element was applied to reduce noise from the images. Then, image threshold was calculated using the Otsu method [20]. 3D Watershed from MorphoLibJ was applied, then 1-voxel dilatation filter. Finally, 3D Object Counter

plugin returned the volume ($V_{p,i}$) of each pore, from which the equivalent pore diameter $\left(6V_{p,i}/\pi\right)^{1/3}$ was calculated.

The produced samples are shown in Fig. 1a-c. Highly monodisperse open cell foams are obtained with several pores sizes (Fig. 1d). The effect of solid volume fraction is shown in Fig. 1c: foam can be described as interconnected struts at small ϕ_s values, spherical pores with small circular apertures are seen for larger ϕ_s values. The decrease of the mean aperture diameter d_o as a function of solid volume fraction is presented in Fig. 1e.

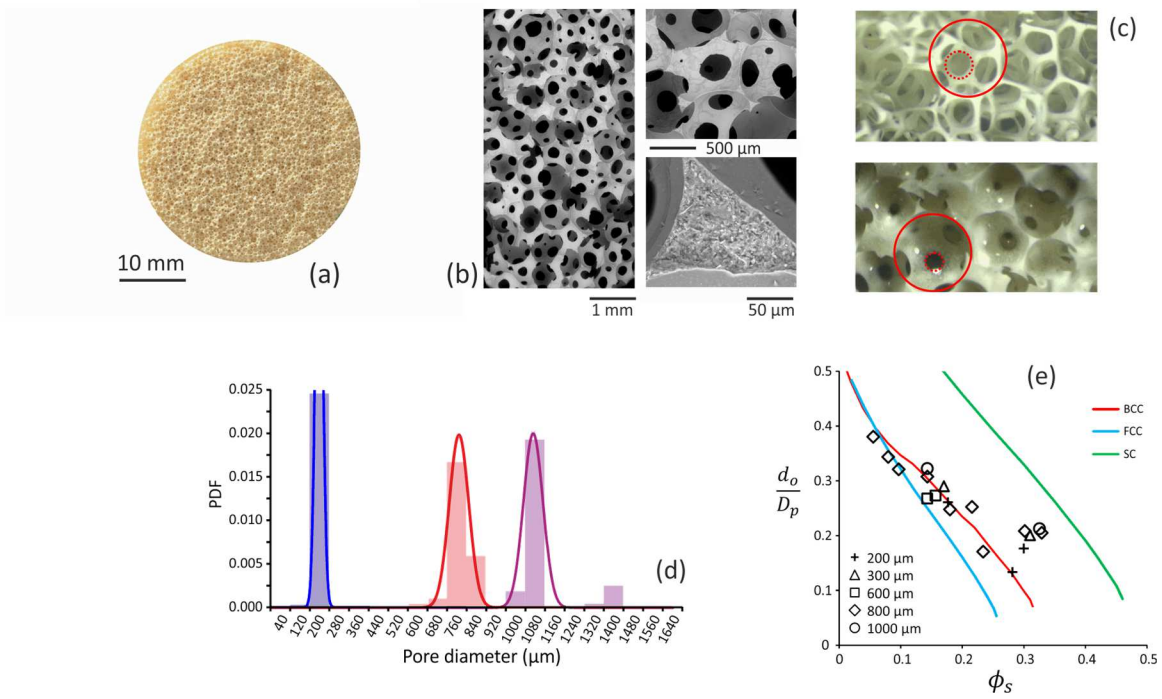

Figure 1: Microstructure of the solid MK foams. (a) Picture of a sample seen from above ($D_p \approx 600$ µm, $\phi_s = 0.2$). (b) SEM images of foam microstructure ($D_p \approx 800$ µm, $\phi_s = 0.15$). (c) Close-up of foam samples revealing the open-cell microstructure and showing pores (continuous lines) and pore apertures (dotted lines). Top: $D_p \approx 800$ µm, $\phi_s = 0.08$; bottom: $D_p \approx 800$ µm, $\phi_s = 0.3$. (d) Volume-weighted pore size distribution (probability density function) obtained from the X-ray tomography method, for three samples. The three Gaussian curves are plotted with mean and standard deviation equal to: 200 µm and 15 µm, 770 µm and 40 µm, 1070 µm and 40 µm. (e) Diameter of apertures d_o (measured using optical microscopy) divided by the pore diameter D_p as a function of solid volume fraction ϕ_s for different pore sizes as indicated. As indicated, the continuous lines correspond to values obtained by using the Surface Evolver software (see the main text for details) for the Kelvin/BCC structure, the FCC structure and the SC structure.

3.4. Fluid permeability

Gas-flow permeability was measured with a home-made setup. A gas flow controller was used to push dry nitrogen through the foam sample (length L and circular cross-section S = 5.3 cm^2) embedded with PTFE ribbon and fitting a cylindrical tube. The pressure difference ΔP across the sample was measured thanks to a manometer. Several measurements were performed as a function of the gas flow rate Q and the foam permeability was deduced from the Darcy law: $k_D = [\mu_a L/S]/[d(\Delta P)/dQ]$, where μ_a = 1.8 10^{-5} Pa.s is the dynamic viscosity of the gas. A typical example is presented in Fig. 3a. Most of the measurements were performed within the identified linear regime characterized by low Reynolds number $Re = \rho(Q/S)D_p/\mu_a \ll 1$, where $\rho \cong 1.2$ kg/m^3. For the largest pore sizes this condition was not fully satisfied so we used the Darcy-Forchheimer equation: $\Delta P/L = \mu_a/k_D \times Q/S + \rho C(Q/S)^2$, where C is the non-Darcy flow coefficient. Darcian permeability was obtained from a quadratic regression performed for the pressure gradient $\Delta P/L$ as a function of Q/S.

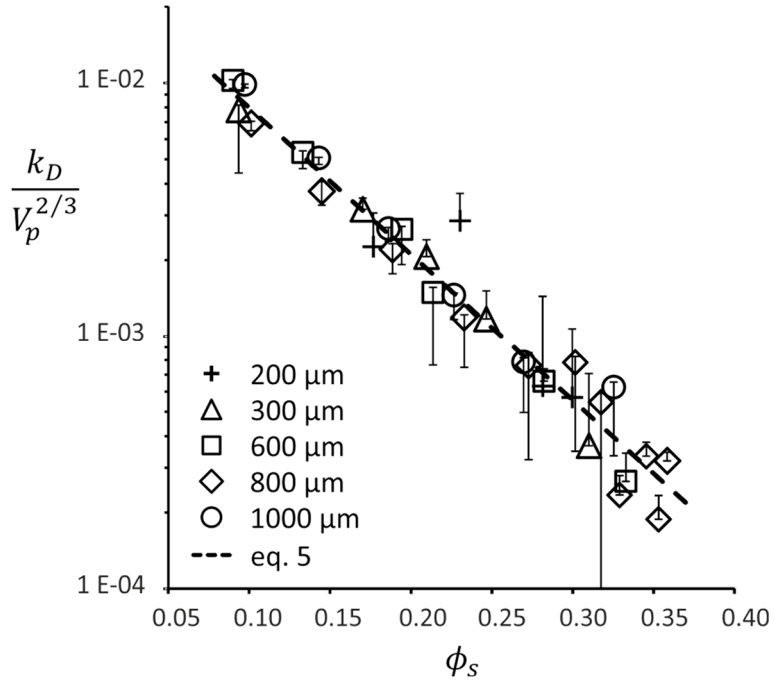

Figure 2: Darcy permeability k_D of the studied foam samples divided by $V_p^{2/3} = \left(\pi D_p^3/6\right)^{2/3}$. Each empty symbol corresponds to a given pore size, as indicated. The dashed line corresponds to eq. 5. Note that permeability vanishes for $\phi_s > \phi_s^* \cong 0.36$, i.e. Random Close Packing of spheres.

Data are presented in Fig. 2. It shown that all the permeability values gather on a straight line when plotting $ln\left(k_D/V_p^{2/3}\right)$ as a function of solid volume fraction ϕ_s, where $V_p = \pi D_p^3/6$ is the pore volume. The data are well described by an exponential function $k_D(D_p, \phi_s)$:

$$\frac{k_D}{V_p^{2/3}} \cong 0.03 \times exp\left(-\frac{\phi_s}{0.073}\right) \qquad \text{(eq. 5)}$$

Note that classical models proposed for packed beds of solid spheres overestimate significantly the foam permeability. For example, at $\phi_s \approx 0.2$, the Carman-Kozeny model [21,22] gives 2 10^{-2} for the dimensionless permeability, while the measured value is 2 10^{-3} (overestimation by factor 10). Actually, available models do not capture the exponential decrease and most of them overestimate our permeability data [23]. In the following we use permeability values given by equation 5.

3.5. Imbibition experiment

Water imbibition was studied by measuring the capillary rise through foam samples. Samples were put in contact with a thin layer (3 mm) of Glucopon solution (1.2 g/L) in a glass container with large cross-section area (800 cm^2). The use of the surfactant solution provided good wetting conditions of the liquid at the walls of the foam skeleton, i.e. the solid/liquid contact angle θ was expected to be such that $cos\theta \cong 1$. The rising front $h(t)$ was followed as a function of time using a camera (see the picture in figure 3). The liquid front was always easy to be distinguished due to appropriate contrast between filled and dry porosities. However, after the expected saturation height for imbibition of the foams pores (the so-called Jurin height), a further increase of the front height could be observed (see Figure 1b) due to the imbibition of the porous skeleton (i.e. geopolymer matrix). Note that this second regime is classical for porous media characterized by two pore sizes [24,25]. Here, the pores of geopolymer matrix are very small [26] and the associate Washburn velocity is negligible compared to the one corresponding to the large pores. As we were mostly interested in the imbibition properties provided by the foam geometry of such foam material, rather than the intrinsic imbibition properties of the geopolymer matrix, in the following we consider only the first and rapid regime.

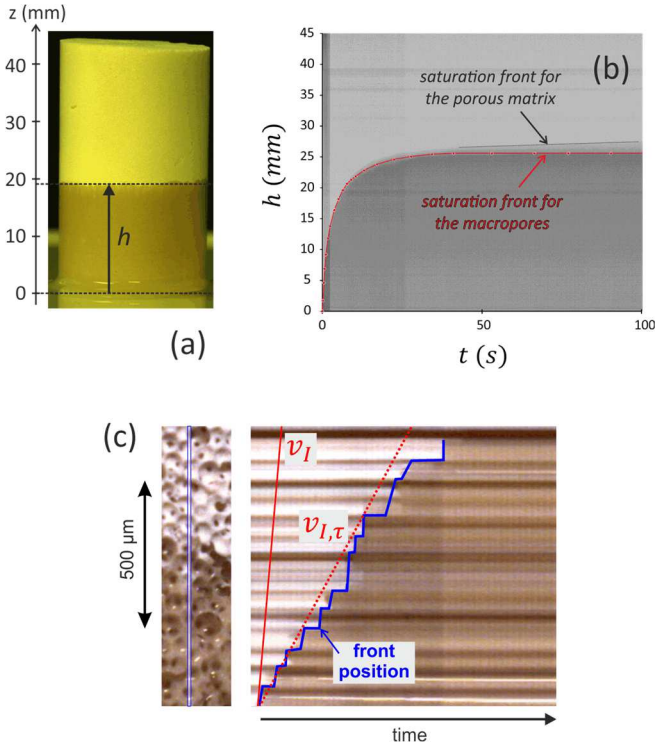

Figure 3: Imbibition experiment. (a) Image of the solid foam sample during imbibition. The sample is put in contact with water solution and the wet front height, h, is followed as a function of time. The front rise is better highlighted through the space-time image shown in (b). The red points and line highlight the water saturation front for the foam pores (macropores). The dotted line highlights the water saturation front in the porous solid skeleton of the foam. The corresponding velocity is small, so the second front is better distinguished after the water front stops in the macropores.
(c) Close-up of the pore filling process during imbibition (left) and corresponding space-time image (right). The blue line shows the positions of the water front.

4. Results and discussion

Imbibition curves

Typical results for liquid imbibition are presented in figure 4a. Note that data are plotted as a function of $t^{1/2}$ in order to identify the Washburn regime. Each curve is characterized by rapid increase which is, indeed, in reasonable agreement with the Washburn behavior. It appears that the velocity v_I depends on both the pore size and solid volume fraction. As expected, the front height saturates at longer times to a value which increases as the pore size decreases. Note that inertial effects are expected to be limited to the very first instants (or heights) of the imbibition process [27], so in the following we restrict our analysis to the Washburn equations (i.e. eqs 1 and 2).

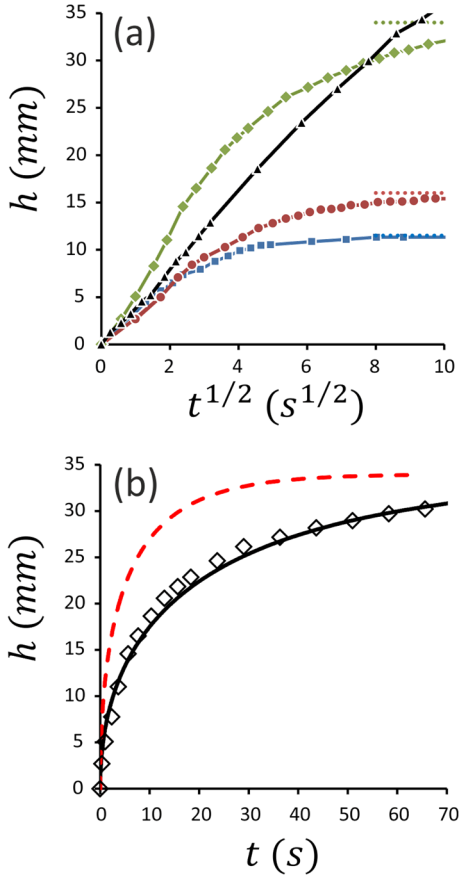

Figure 4: Typical imbibition curves, i.e. capillary rise height as a function of time. (a) Height h as a function of $t^{1/2}$ for samples. Squares: D_p = 1030 µm and ϕ_s = 0.33; Circles: D_p = 630 µm and ϕ_s = 0.28; Diamonds: D_p = 300 µm and ϕ_s = 0.17; Triangles: D_p = 195 µm and ϕ_s = 0.18. The dotted lines corresponds observed saturation heights. (b) Height h as a function of time for sample characterized by D_p = 300 µm and ϕ_s = 0.17. Solid line corresponds to equation 2 with parameters: ΔP_c = 333 Pa (equivalently h_∞ = 34 mm), k_I = 6 10^{-11} m^2. The dashed line corresponds to equation 2 with parameters: ΔP_c = 333 Pa (equivalently h_∞ = 34 mm), $k_I = k_D$ = 22.6 10^{-11} m^2.

Equation 2 is now compared against experimental values $h(t)$, as shown in Fig. 4b. Note that the value for the saturation height h_∞ sets the value for ΔP_c, so fitting equation 2 to our data provides the value for the second parameter, that is, foam permeability k_I. Following such a procedure, we obtain values for ΔP_c and k_I, as presented in Figs 5a&b respectively. Note that the saturation height with $D_p \approx$ 200 µm samples, was found to be larger than the sample heights so the capillary pressure could not be measured. For such cases however, it was assumed that the values for the dimensionless capillary pressure are similar to values measured for other samples (within the spread observed for the data in Fig. 5a – see the red crosses), so the corresponding permeability was also deduced by fitting the theoretical curve to the data.

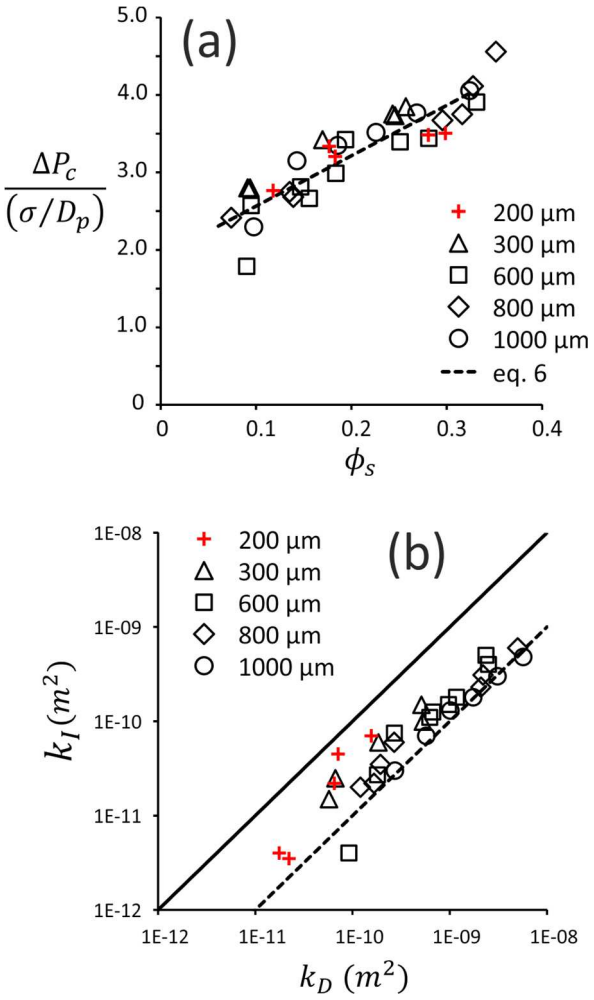

Figure 5: (a) Capillary pressure ΔP_c divided by σ/D_p as a function of solid volume fraction ϕ_s. Each symbol corresponds to a given pore size, as indicated (crosses correspond to samples with pore size close to 200 µm, for which the dimensionless capillary pressure could not be measured but was assumed to be similar to other samples). The dashed line corresponds to eq. 6. (b) Foam permeability k_I as deduced from imbibition experiments (see eq. 1) as a function of foam permeability, k_D as measured by Darcy experiment (Fig. 2). Each symbol corresponds to a given pore size, as indicated. The solid line corresponds to $k_I = k_D$. The dashed line corresponds to $k_I = k_D/10$.

Capillary pressure

Let us first discuss values obtained for the capillary pressure ΔP_c. It is shown in Fig. 5a that plotting the dimensionless pressure $\Delta P_c/(\sigma/D_p)$ for all the studied pore sizes allows for a single curve to be obtained as a function of solid volume fraction ϕ_s. This pressure appears to be an increasing function of ϕ_s, from $\Delta P_c/(\sigma/D_p) \approx 2$ for $\phi_s \approx 0.05$ to $\Delta P_c/(\sigma/D_p) \approx 4$ for $\phi_s \approx 0.35$, and it is reasonably described by an affine function (which is obtained by a linear regression):

$$\Delta P_c \approx \frac{\sigma}{D_p}(1.95 + 6.4\phi_s) \quad \text{(eq. 6)}$$

Note that the maximal value for ΔP_c, i.e. $4\sigma/D_p$, corresponds to $|1/\bar{r}| \approx 2/D_p$, which means that the radius of curvature for the liquid-gas interface is approximately equal to the pore radius. This can be understood from the spherical shape of the pores surface for such ϕ_s values (see Fig. 1c). As ϕ_s decreases, the size of the apertures connecting the pores increases as well and the resulting pore surface is increasingly open. For the smallest ϕ_s values, the foam solid structure mainly consists in an assembly of struts. Such structure has some similarity with bundles of cylindrical fibers as studied by Princen [28]. Therefore, the decrease observed for the capillary pressure is expected to be related to the evolution of the pore geometry. In order to quantify this effect, we propose to consider the middle cross-section A of a single representative pore, such as the one shown in Fig. 6a. Mechanical equilibrium for the liquid within the structure is reached when the liquid weight, $\rho h A g$, is supported exactly by the surface tension along the wetted perimeter ℓ of the pore surface, $\sigma\ell$. As $\rho g h = \Delta P_c$ at equilibrium, the dimensionless capillary pressure writes: $\Delta P_c/(\sigma/D_p) = \ell D_p/A$.

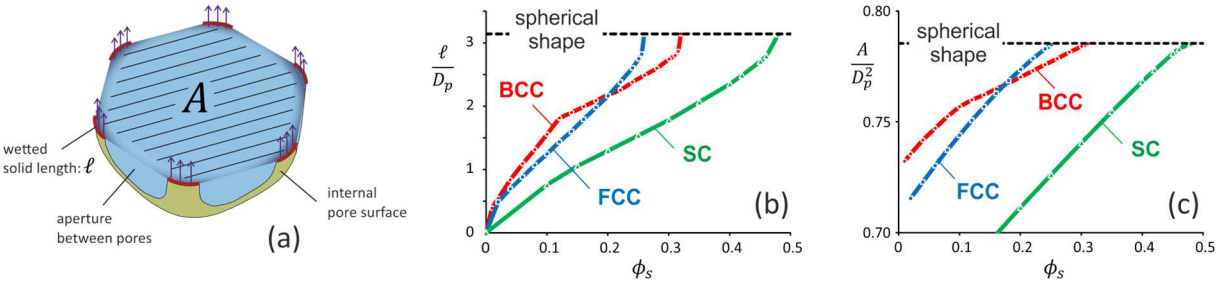

Fig. 6: (a) Sketch of single representative foam pore (cut at the middle cross-section for clarity). In each pore, surface tension acting at the solid surface (shown by the arrows) supports the column of liquid beneath the interface. (b) Wetted solid length ℓ divided by D_p as a function of solid volume fraction for three ideal foam structures: FCC, BCC (Kelvin) and SC. (c) Pore cross section A divided by D_p^2 for three ideal foam structures: FCC, BCC (Kelvin) and SC.

Values for ℓ and A have been obtained by numerical simulations (see Fig. 6b&c) for several foam structures: FCC (Face-Centered Cubic), BCC (Body-Centered Cubic, also called Kelvin cells) and SC (Simple Cubic). Fine convergence of our numerical simulations was obtained by using the Surface Evolver – Fluid Interface Tool (SE-FIT). First of all, each structure shows spherical pores characterized

by $\ell/D_p = \pi$ and $A/D_p^2 = \pi/4$ for a critical volume fraction ϕ_s such that $\phi_s^{fcc} = 0.26$, $\phi_s^{bcc} = 0.32$ and $\phi_s^{sc} = 0.48$. For smaller ϕ_s values, ℓ decrease from πD_p to 0 whereas A decreases weakly. Note the particular behavior for the BCC structure around $\phi_s \cong 0.11$ due to the transition from 14 apertures (Kelvin cell) for $\phi_s \lesssim 0.11$ to 8 apertures for $\phi_s \gtrsim 0.11$ [29]. Using values presented in Figs 6b&c, the dimensionless capillary pressure is calculated for the three structures and the results are plotted in Fig. 7 against experimental data. The FCC structure cannot be used to describe our results for $\phi_s > 0.26$ and the SC structure appears to underestimate significantly the data. In contrast, the BCC structure describes reasonably well the measured capillary pressures over the studied range of solid volume fraction. It is to say that the Kelvin structure is often used as ideal structure in order to evaluate foam properties such as drainage [16], mechanics [30] or acoustics [31]. Note that more general models have been proposed to describe the capillary pressure on porous media. For example, Masoodi & Pillai [32] proposed the following expression: $\Delta P_c = \phi_s \sigma/(1-\phi_s)\Gamma$, where Γ is the volume-to-surface area of the solid matrix. The corresponding dimensionless capillary pressure thus writes $\Delta P_c/(\sigma/D_p) = D_p A_s/(1-\phi_s)$ where A_s is the specific surface area, i.e. the surface area of the solid matrix in contact with the fluid divided by the total volume of porous material. Such a parameter can be found elsewhere [16,33] for the BCC structure. The calculated values for $\Delta P_c/(\sigma/D_p)$ are plotted in Fig. 7 and show significant overestimation of our experimental data.

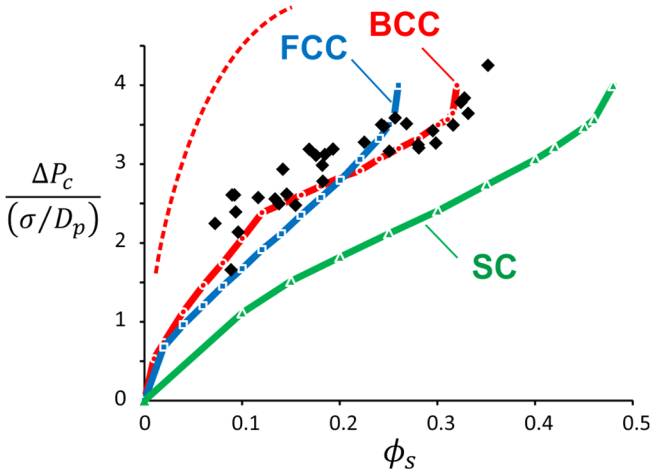

Fig. 7: Capillary pressure ΔP_c divided by σ/D_p as a function of solid volume fraction ϕ_s. Black diamonds correspond to experimental data presented in Fig. 5a. Solid lines correspond to equation $\Delta P_c/(\sigma/D_p) = \ell D_p/A$ with ℓ and A given by Fig. 6 for the three studied foam structures: FCC, BCC (Kelvin) and SC. The dotted line corresponds to equation $\Delta P_c/(\sigma/D_p) = D_p A_s/(1-\phi_s)$, where A_s is the specific surface area for the BCC structure.

Apparent permeability

For an ideal porous material, it is expected that $k_I = k_D = k$. Here, permeability values k_I deduced from imbibition results (see Fig. 5b) were found to be one order of magnitude smaller than measured Darcy permeability k_D. In other words, using the measured foam permeability values in equation 2 would give imbibition velocity 10 times larger than the measured velocity (see Fig. 4b). In order to understand this discrepancy we record movies from the magnified surface of the sample (at the scale of ~10 pores, see Fig. 3c). This reveals a halting pore-filling process: from pore to pore, the capillary ascending motion pauses regularly (see the space-time image). It is recognized that interface motions can be slowed down or even stopped by passing through pore junctions [34] or through capillaries with significant expansion of the cross-section [35,36] and such intermittent front rise has been observed in similar cellular materials [25]. In order to reconcile k_I and k_D values, we introduce an additional time τ corresponding to the time spent by the fluid to pass through the aperture between two neighbor pores. Note that the vertical motion in pores is still considered as mainly governed by the balance between capillary effects and Darcy's law (leading to eqs 1 and 4). Therefore, the average time for the interface to travel a length D_p is equal to $D_p/v_I + \tau$, and the modified imbibition velocity is:

$$v_{I,\tau} = \frac{D_p}{\frac{D_p}{v_I}+\tau} = \frac{D_p}{\frac{D_p \phi \mu h}{k_D \Delta P_c}+\tau} \quad \text{(eq. 7)}$$

The physical mechanism involved in time τ is not known so we turn to a phenomenological approach to identify a functional form that allows for data to be understood with eq. 7. Our results for imbibition show a Washburn behavior for $h \ll h_\infty$, which suggests that τ is proportional to h: $\tau = f\left(\phi_s, D_p/\kappa^{-1}\right) \times \mu h/\sigma$, where $\kappa^{-1} = \sqrt{\sigma/\rho g}$ is the capillary length and f is a dimensionless function. As $v_{I,\tau} \equiv k_I \Delta P_c/\phi \mu h$, the apparent permeability k_I writes as a function of $f\left(\phi_s, D_p/\kappa^{-1}\right)$:

$$k_I = \left(\frac{1}{k_D} + \frac{\Delta P_c}{D_p \phi \sigma} f\right)^{-1} \quad \text{(eq. 8)}$$

Note that the term $\phi \sigma D_p/\Delta P_c f$ in eq. 8 can be considered as an additional permeability associated in series with the Darcy permeability. We have sought for $f\left(\phi_s, D_p/\kappa^{-1}\right)$ as a power law function, that is, $f = \alpha\left(D_p/\kappa^{-1}\right)^x \phi_s^y$, where α is a numerical constant. As shown in Fig. 8 it is possible to obtain parameters (α, x, y) such that eq. 8 is fulfilled for all the values k_I and k_D: $f \sim \left(D_p/\kappa^{-1}\right)\phi_s^{3/2}$.

Equivalently, the time τ expresses as $\tau/(\mu D_p/\sigma) \sim \phi_s^{3/2}\, h/\kappa^{-1}$ and it is expected to be related to the size of the apertures as well as the geometry of the surrounding borders. The porosity of the geopolymer matrix may also influence the time τ. A dedicated study of the interface breakthrough should be performed at the scale of the single aperture in order to understand and clarify the reported dependence for time τ.

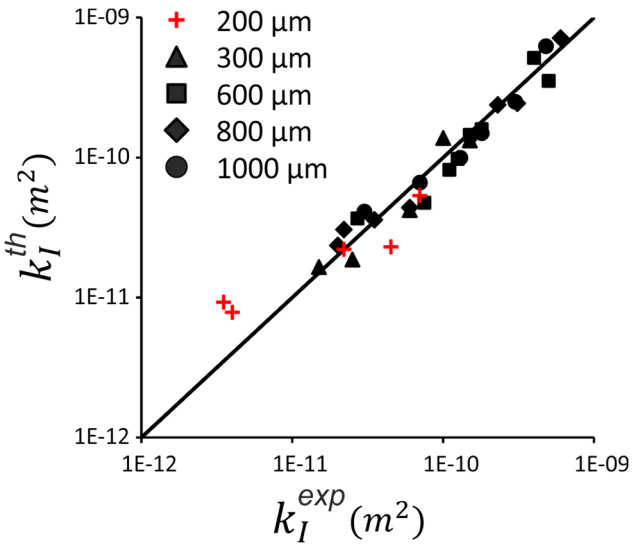

Figure 8: Permeability values given by eq. 7 as a function of permeability values deduced from imbibition experiments. In eq. 8, k_D values are given by eq. 5, ΔP_c values are presented in Fig. 5a, and $f = \alpha(D_p/\kappa^{-1})\phi_s^{3/2}$ with α = 34 10³. Each symbol corresponds to a given pore size, as indicated.

5. Conclusion

Solid foam samples were produced with monodisperse pore sizes and controlled pore volume fractions. Vertical imbibition experiments were performed in order to measure both the imbibition rate and the saturation height. Saturation heights allowed us to deduce the driving capillary pressure in the foam structures, showing values inversely proportional to pore size. Moreover, the capillary pressure was found to decrease as a function of the pore volume fraction, which was understood by the evolution of the pore geometry, from spherical shape of the pore surface, for pore volume fractions close to 60%, to increasingly open pore surface for higher pore volume fractions. Moreover, these experimental values were found to be consistent with values calculated by adapting the approach proposed by Princen [28] for bundles of cylindrical fibers. Here, the calculation based on the ideal BCC (Kelvin) foam structure was found to provide values very close to experimental values.

Eventually, the dimensionless values reported in this paper for the capillary pressure can be used easily to estimate saturation of liquids in various foamed materials. We recall that experiments were conducted within good wetting conditions, i.e. $\theta \cong 0$. For non-vanishing contact angle, one can anticipate that the driving capillary pressure is decreased by a factor $cos\theta$, i.e. $\Delta P_c \approx \sigma cos\theta(1.95 + 6.4\phi_s)/D_p$ can be used in eq. 4 for example. This behavior is expected for contact angles below the critical value θ_c, for which ΔP_c = 0. Further study could be focused on the the effect of contact angle, and more precisely, to the determination of θ_c.

The measured imbibition rate was found to be qualitatively compatible with the Washburn theory [11–13], i.e. the imbibition length is proportional to the square root of time, but it is one order of magnitude smaller than the values predicted from the Darcy foam permeability measured on the same samples. Our result clearly shows that the use of the classical Washburn theory can induce overestimation of the imbibition rate by factor 10. Overestimation by factor 100 can even be reached if appropriate values for both foam permeability (eq. 5) and foam capillary pressures (eq. 6) are not used.

In the last part of this work we tried to reconcile theory with measured imbibition rates. From video-microscopy performed at the pore scale, we identify an excess time spent by the liquid-gas interface at connections between pores and we introduced this excess time in the expression of the imbibition velocity. This excess time is believed to be related to the particular motions for the interface when it reaches pore junctions [34] or areas characterized by sharp changes of channel cross-section [35,36]. A dedicated study should be performed at the scale of a single pore connection in order to clarify this effect. Here we turned to a phenomenological approach and an empirical expression was provided for the excess time. Additionally, studies should be performed at both pore scale and sample scale with several couples liquid/solid in order to quantify the effect of contact angle as it becomes close to the critical contact angle θ_c.

Expressions provided for both foam permeability, foam capillary pressure and excess time, can be used to estimate imbibition rates in solid foams. For example, this would be helpful to control foam imbibition and impregnation processes involved in the design of foamed materials with improved functional properties, such as superhydrophobicity [5,6], antibacterial [7], electrical [8] or fire-safe [9] properties.

Acknowledgments

The authors thank P. Aimedieu (at Navier Laboratory) for technical support with the X-ray tomography. This work has benefited from French government Grant managed by the Agence Nationale de la Recherche [Grant number ANR-13-RMNP-0003-01].

References

[1] L.J. Gibson, M.F. Ashby, Cellular Solids: Structure and Properties, Cambridge University Press, Cambridge, 1997.

[2] X. Zhang, Z. Li, K. Liu, L. Jiang, Bioinspired multifunctional foam with self-cleaning and oil/water separation, Advanced Functional Materials. 23 (2013) 2881–2886. doi:10.1002/adfm.201202662.

[3] L. Luo, X. Chen, Y. Wang, J. Yue, Z. Du, X. Huang, X.Z. Tang, Bio-inspired modification of silicon carbide foams for oil/water separation and rapid power-free absorption towards highly viscous oils, Ceramics International. 44 (2018) 12021–12029. doi:10.1016/j.ceramint.2018.03.196.

[4] Z. Hardy, V.A. Jideani, Foam-mat drying technology: A review, Critical Reviews in Food Science and Nutrition. 57 (2017) 2560–2572. doi:10.1080/10408398.2015.1020359.

[5] Z. Zhang, H. Wang, Y. Liang, X. Li, L. Ren, Z. Cui, One-step fabrication of robust superhydrophobic and superoleophilic surfaces with self- cleaning and oil / water separation function, Scientific Reports. 8:3869 (2018) 1–12. doi:10.1038/s41598-018-22241-9.

[6] X. Gao, J. Zhou, R. Du, Z. Xie, S. Deng, R. Liu, Robust Superhydrophobic Foam : A Graphdiyne-Based Hierarchical Architecture for Oil / Water Separation, Advanced Materials. 28 (2015) 168–173. doi:10.1002/adma.201504407.

[7] P. Jain, T. Pradeep, Potential of Silver Nanoparticle-Coated Polyurethane Foam As an Antibacterial Water Filter, Biotechnology and Bioengineering. 90 (2005) 59–63. doi:10.1002/bit.20368.

[8] X. Xinzhao, L. Guoming, L. Dongyan, S. Guoxin, Y. Rui, Electrically conductive graphene-coated polyurethane foam and its epoxy composites, Composites Communications. 7 (2018) 1–6. doi:10.1016/j.coco.2017.11.003.

[9] H. Xie, X. Lai, Y. Wang, H. Li, X. Zeng, A green approach to fabricating nacre-inspired nanocoating for super-efficiently fire-safe polymers via one-step self-assembly, Journal of Hazardous Materials. 365 (2019) 125–136. doi:10.1016/j.jhazmat.2018.10.099.

[10] C. Ma, B. Chen, Properties of foamed concrete containing water repellents, Construction and Building Materials. 123 (2016) 106–114. doi:10.1016/j.conbuildmat.2016.06.148.

[11] J.M. Bell, F.K. Cameron, The flow of liquids through capillary spaces, J. Phys. Chem. 10 (1906) 658–674.

[12] R. Lucas, Ueber das Zeitgesetz des kapillaren Aufstiegs von Flüssigkeiten, Kolloid-Zeitschrift. 23 (1918) 15–22.

[13] E.W. Washburn, The dynamics of capillary flow, Physical Review. 17 (1921) 273–283.

[14] F.A.L. Dullien, Porous media : fluid transport and pore structure, Academic Press, 1991.

[15] A. Kaddami, O. Pitois, A physical approach towards controlling the microstructure of

metakaolin-based geopolymer foams, Cement and Concrete Research. 124 (2019) 105807. doi:10.13140/RG.2.2.30318.87367.

[16] I. Cantat, S. Cohen-Addad, F. Elias, F. Graner, R. Höhler, O. Pitois, F. Rouyer, Foams: Structure and Dynamics, Oxford University Press, Oxford, 2013.

[17] F.G. Gandolfo, H.L. Rosano, Interbubble Gas Diffusion and the Stability of Foams, Journal of Colloid and Interface Science. 194 (1997) 31–36. doi:10.1006/jcis.1997.5067.

[18] C.T. Rueden, J. Schindelin, M.C. Hiner, B.E. DeZonia, A.E. Walter, E.T. Arena, K.W. Eliceiri, ImageJ2: ImageJ for the next generation of scientific image data, BMC Bioinformatics. 18 (2017) 529. doi:10.1186/s12859-017-1934-z.

[19] D. Legland, I. Arganda-Carreras, P. Andrey, MorphoLibJ: integrated library and plugins for mathematical morphology with ImageJ, Bioinformatics. 32 (2016) 3532–3534. doi:10.1093/bioinformatics/btw413.

[20] N. Otsu, A Threshold Selection Method from Gray-Level Histograms, IEEE Transactions on Systems, Man, and Cybernetics. 9 (1979) 62–66. doi:10.1109/TSMC.1979.4310076.

[21] P.C. Carman, Fluid flow through granular beds, Trans. Instn Chem. Engrs. 15 (1937) 150–166. doi:10.1016/S0263-8762(97)80003-2.

[22] J. Kozeny, Ueber kapillare Leitung des Wassers im Boden, Sitzungsber Akad. Wiss. 136 (1927) 271–306.

[23] P. Kumar, F. Topin, State-of-the-Art of Pressure Drop in Open-Cell Porous Foams: Review of Experiments and Correlations, Journal of Fluids Engineering. 139 (2017) 111401. doi:10.1115/1.4037034.

[24] J. Bico, U. Thiele, D. Quéré, Wetting of textured surfaces, Colloids and Surfaces A: Physicochemical and Engineering Aspects. 206 (2002) 41–46.

[25] T. Lerouge, O. Pitois, D. Grande, B. Le Droumaguet, P. Coussot, Synergistic actions of mixed small and large pores for capillary absorption through biporous polymeric materials, Soft Matter. 14 (2018) 8137–8146. doi:10.1039/C8SM01400K.

[26] J. Davidovits, Geopolymers, Journal of Thermal Analysis. 37 (1991) 1633–1656. doi:10.1007/BF01912193.

[27] N. Fries, M. Dreyer, The transition from inertial to viscous flow in capillary rise, Journal of Colloid and Interface Science. 327 (2008) 125–128. doi:10.1016/j.jcis.2008.08.018.

[28] H.M. Princen, Capillary phenomena in assemblies of parallel cylinders. II. Capillary rise in systems with more than two cylinders, Journal of Colloid and Interface Science. 30 (1969) 359–371.

[29] D.L. Weaire, S. Hutzler, The Physics of Foams, Oxford University Press, Oxford, 2001.

[30] W.Y. Jang, S. Kyriakides, A.M. Kraynik, On the compressive strength of open-cell metal foams with Kelvin and random cell structures, International Journal of Solids and Structures. 47 (2010) 2872–2883. doi:10.1016/j.ijsolstr.2010.06.014.

[31] V.H. Trinh, V. Langlois, J. Guilleminot, C. Perrot, Y. Khidas, O. Pitois, Tuning membrane content of sound absorbing cellular foams: Fabrication, experimental evidence and multiscale numerical simulations, Materials and Design. 162 (2019) 345–361. doi:10.1016/j.matdes.2018.11.023.

[32] R. Masoodi, K.M. Pillai, A general formula for capillary suction-pressure in porous media, Journal of Porous Media. 15 (2012) 775–783. doi:10.1615/JPorMedia.v15.i8.60.

[33] O. Pitois, E. Lorenceau, N. Louvet, F. Rouyer, Specific surface area model for foam

permeability, Langmuir. 25 (2009) 97–100. doi:10.1021/la8029616.

[34] Z. Sadjadi, M. Jung, R. Seemann, H. Rieger, Meniscus arrest during capillary rise in asymmetric microfluidic pore junctions, Langmuir. 31 (2015) 2600–2608. doi:10.1021/la504149r.

[35] D. Erickson, D. Li, C.B. Park, Numerical simulations of capillary-driven flows in nonuniform cross-sectional capillaries, Journal of Colloid and Interface Science. 250 (2002) 422–430. doi:10.1006/jcis.2002.8361.

[36] H. Mehrabian, P. Gao, J.J. Feng, Wicking flow through microchannels, Physics of Fluids. 23 (2011) 1–14. doi:10.1063/1.3671739.

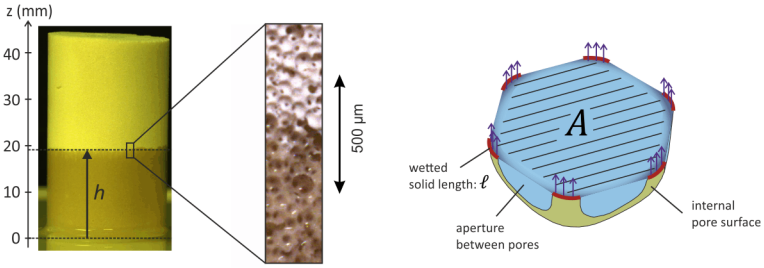

The measured rise velocity of liquid in solid foam is one order of magnitude smaller than the predicted value. This deviation is attributed to the excess time spent by the liquid-gas interface at connections between pores.